J. Fluid Mech. (2011), *vol.* 682, *pp.* 415–433. © Cambridge University Press 2011
doi:10.1017/jfm.2011.235

Spreading and breakup of a compound drop on a partially wetting substrate

PENG GAO[1]† AND JAMES J. FENG[1,2]‡

[1]Department of Chemical and Biological Engineering, University of British Columbia, Vancouver, BC V6T 1Z3, Canada

[2]Department of Mathematics, University of British Columbia, Vancouver, BC V6T 1Z2, Canada

(Received 19 August 2010; revised 29 March 2011; accepted 17 May 2011; first published online 1 July 2011)

The spreading of a compound drop on a partially wetting solid substrate is numerically simulated using a diffuse-interface method. Compared with a simple drop, the spreading of a compound drop exhibits much more complex behaviour. Depending on the core–shell size ratio and the substrate wettability, various flow regimes are identified in which the interfacial morphology evolves in distinct ways. A phase diagram is constructed in the parameter space of the core–shell size ratio and the wetting angle. For relatively small inner drops, the outer interface does not rupture during the spreading and the inner drop either remains suspended and encapsulated or attaches onto the substrate. Otherwise, the compound drop spontaneously breaks up and releases the inner drop into the ambient fluid. Several breakup scenarios are observed depending on the location of the initial rupture. In some regimes, the wetting of the substrate by one fluid can entrap secondary drops of the other, which can either attach to the substrate or stay suspended. The viscosity ratio mainly affects the spreading rate and plays a minor role in the morphology evolution.

Key words: breakup/coalescence, contact lines

1. Introduction

Compound drops with a smaller droplet encapsulated in a fluid shell are encountered in a variety of industrial processes, such as heat exchange, separation and materials processing (Johnson & Sadhal 1985; Sadhal, Ayyaswamy & Chung 1997). Dispersion of a large number of compound drops in a continuous phase produces a double or multiple emulsion. The oil-in-water-in-oil (O/W/O) and water-in-oil-in-water (W/O/W) types are the most common with wide-ranging applications, e.g. as carriers in targeted drug delivery (Engel, Riggi & Fahrenba 1968; Garti & Bisperink 1998; Laugel *et al.* 2000). In biomechanics, the compound drop model has been used to describe the rheology of leukocytes (Hochmuth *et al.* 1993; Kan *et al.* 1998).

Early work dealt with the hydrostatics of compound drops and their motion in a quiescent medium (Johnson & Sadhal 1985; Sadhal *et al.* 1997). These studies typically assume a spherical or nearly spherical drop shape, and sought approximate analytical solutions at small Reynolds numbers (Rushton & Davies 1983; Sadhal & Oguz 1985).

† Present address: Department of Modern Mechanics, University of Science and Technology of China, Hefei, Anhui 230026, China.

‡ Email address for correspondence: jfeng@math.ubc.ca

https://doi.org/10.1017/jfm.2011.235 Published online by Cambridge University Press

An interesting result observed by Rushton & Davies (1983) is that a compound drop translates like a solid sphere when the liquid shell is very thin. Kawano, Shirai & Nagasaka (2007) performed experiments as well as numerical simulations on the deformation of compound drops moving at intermediate Reynolds numbers. The calculated drag coefficients were in good agreement with experimental observations.

More recent work investigated the behaviour of compound drops in an external flow field. Two kinds of flows have been examined so far: extensional flows (Stone & Leal 1990; Kan *et al.* 1998) and shear flows (Stroeve & Varanasi 1984; Smith, Ottino & de la Cruz 2004). Both flows can lead to significant drop deformation and even breakup at sufficiently high strain rates. In an extensional flow, the two interfaces typically deform in opposite ways owing to the recirculation developed inside the drop; when the outer interface becomes prolate, the core becomes oblate. Of particular interest is the breakup of compound drops in these flows, which may be desirable for example in the release of drugs (Muguet *et al.* 2001) or undesirable in extraction using double emulsions (Stroeve & Varanasi 1984). Depending on the radius ratio between the two interfaces, Stone & Leal (1990) noted two breakup scenarios in extensional flows, one with the inner drop deforming and protruding onto the outer interface and the other with the outer interface squeezing a mildly deformed inner one. Smith *et al.* (2004) showed that the breakup of a compound drop in a shear flow can generate a range of topological morphologies, which typically consist of a series of daughter compound drops.

Less work has been done on the hydrodynamics of compound drops in the presence of a solid wall. The wall effect is important in the transit of a cell into a capillary (Yap & Kamm 2005), the generation of monodisperse double emulsions using microfluidic devices (Okushima *et al.* 2004; Utada *et al.* 2005) and diesel engine combustors with blended fuels (Chiu & Lin 2005). Zhou, Yue & Feng (2008) performed numerical simulations of a compound drop through a contraction in a pipe flow, where the drop does not make contact with the wall. In this case, the wall only acts as a boundary for the flow and its wetting property does not enter the dynamics. The wettability does come into play in situations such as the adhesion of a cell to a pipet and direct-contact heat exchangers. However, little is known about the interaction between a compound drop and a solid substrate when they are in contact. Mahadevan, Adda-Bedia & Pomeau (2002) considered the statics of compound droplets on a rigid substrate. Chiu & Lin (2005) carried out experiments on a compound drop impinging on a solid surface and found that secondary drops can be created. Bird *et al.* (2010) studied the breakup of a soap bubble, which is a thin-shelled compound drop, on a solid substrate and observed a cascade of ruptures that generate smaller and smaller daughter bubbles. In the last two studies, the dynamics was dominated by inertial effects and the wetting properties of the substrate were not addressed.

In the present work, we perform numerical simulations of the spreading of a compound drop on a partially wetting substrate. The main purpose is to explore various scenarios of morphological change of a compound drop during its spreading. We show that the spreading and rupture of a compound drop are much more complex and interesting than for a simple one, which would assume an equilibrium shape of a spherical cap (Bonn *et al.* 2009). In contrast, a compound drop can spontaneously break up over a solid substrate without any help of an imposed flow.

2. Theory and numerical method

We consider the spreading of a two-component compound drop that is deposited just above a partially wetting substrate (figure 1*a*). The inner drop and the ambient

https://doi.org/10.1017/jfm.2011.235 Published online by Cambridge University Press

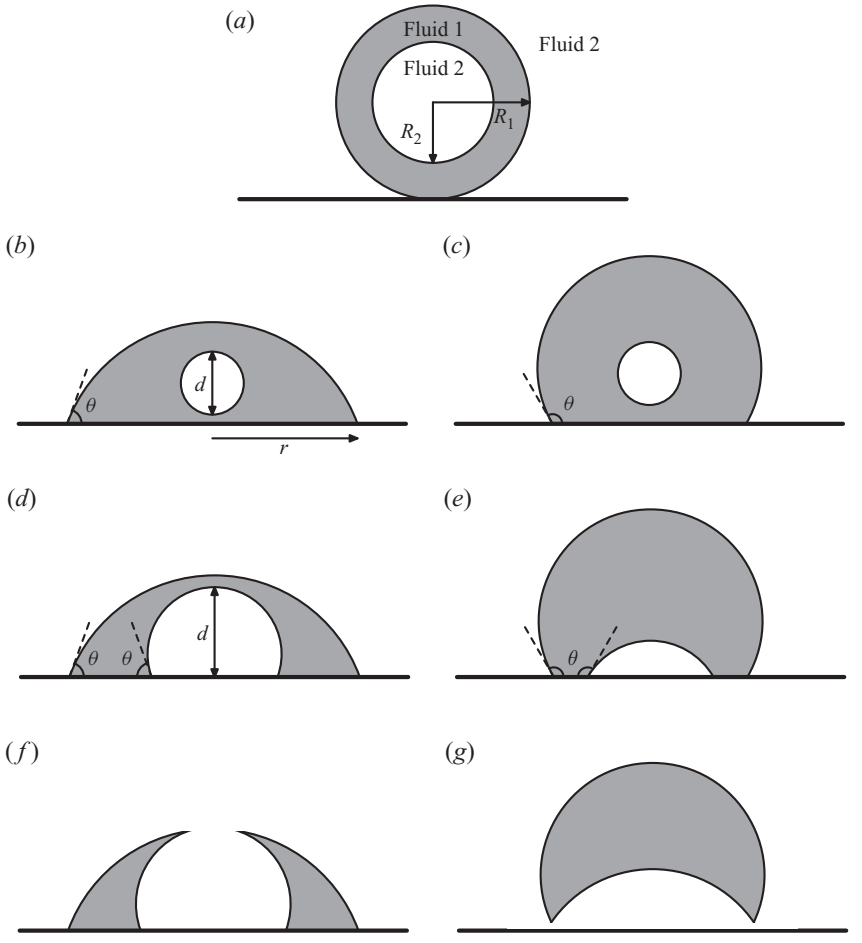


FIGURE 1. Schematic representation of the initial condition of a compound drop on a solid substrate (a) and possible flow regimes of subsequent spreading. Both wetting (b,d,f) and non-wetting (c,e,g) cases are illustrated. (b,c) Regime I: the inner drop remains encapsulated by fluid 1. (d,e) Regime II: the inner drop makes contact with the substrate. (f,g) Regime III: the compound drop breaks up when the inner drop is too large.

fluid are the same as in W/O/W or O/W/O double emulsions. Initially, the outer and inner interfaces are concentrical spheres of radius R_1 and R_2, respectively. Thus, the dynamic process can be studied in an axisymmetric set-up. The shell is occupied by fluid 1 with viscosity μ_1, and the core and the ambient space contain fluid 2 with viscosity μ_2; both fluids are Newtonian, incompressible and mutually immiscible. In this work, we focus on the dynamics of micrometre-size drops, for which inertia and gravity can be safely neglected while viscosity and capillarity dominate the flow.

A diffuse-interface model is employed to describe the interfacial deformation and the moving contact line (Jacqmin 2000; Qian, Wang & Sheng 2006; Yue, Zhou & Feng 2010). One of the advantages of the diffuse-interface method is its ease in handling topological changes such as interfacial coalescence and rupture, where short-range molecular forces come into play and the sharp-interface Navier–Stokes description fails (Yue *et al.* 2005). In this model, the fluid–fluid interface is treated as a thin diffuse layer within which the two fluids mix to store a mixing free energy related to

https://doi.org/10.1017/jfm.2011.235 Published online by Cambridge University Press

the interfacial tension. We introduce a phase-field variable ϕ such that $\phi = 1$ in the bulk of fluid 1 and $\phi = -1$ in the bulk of fluid 2. Across the interface, ϕ varies steeply yet smoothly, and the position of the interface is given by the contour of $\phi = 0$. The advection and diffusion of ϕ is governed by the Cahn–Hilliard equation

$$\frac{\partial \phi}{\partial t} + \boldsymbol{v} \cdot \nabla \phi = \nabla \cdot (\gamma \nabla G), \tag{2.1}$$

where $\boldsymbol{v}$ is the flow velocity, t is time and γ is called the mobility; $G = \lambda[-\nabla^2 \phi + (\phi^2 - 1)\phi/\epsilon^2]$ is the chemical potential, with λ being the mixing energy density and the capillary width ϵ characterizing the thickness of the diffuse interface. By integrating the mixing energy across the interface associated with an analytical equilibrium profile ϕ, one can obtain the interfacial tension σ as

$$\sigma = \frac{2\sqrt{2}}{3}\frac{\lambda}{\epsilon}. \tag{2.2}$$

Since inertia is neglected, the flow is governed by the continuity equation and the Stokes equation

$$\nabla \cdot \boldsymbol{v} = 0, \tag{2.3}$$

$$-\nabla p + \nabla \cdot [\mu(\nabla \boldsymbol{v} + (\nabla \boldsymbol{v})^{\mathrm{T}})] + G \nabla \phi = 0. \tag{2.4}$$

Note that the momentum equation is modified by the addition of the term $G\nabla\phi$ representing the contribution of the interfacial force. The viscosity $\mu(\phi)$ is defined as

$$\mu = \tfrac{1}{2}(1 + \phi)\mu_1 + \tfrac{1}{2}(1 - \phi)\mu_2, \tag{2.5}$$

which recovers the viscosity μ_1 or μ_2 in the bulk.

The computational domain is a $4R_1 \times 4R_1$ square on the meridian plane, its left side being the axis of symmetry. For the velocity $\boldsymbol{v}$, we impose symmetric boundary conditions on the axis, no-slip and no-penetration on the substrate, and vanishing stress on the outer boundary of the domain. For the phase field ϕ, the no-flux condition $\boldsymbol{n} \cdot \nabla G = 0$ is used along all boundaries, $\boldsymbol{n}$ being the outward unit normal vector. In addition, we set

$$\lambda \boldsymbol{n} \cdot \nabla \phi = \begin{cases} -f_w'(\phi) & \text{on the substrate,} \\ 0 & \text{elsewhere,} \end{cases} \tag{2.6}$$

where f_w is the wall free energy (Jacqmin 2000; Yue *et al.* 2010)

$$f_w(\phi) = -\sigma \cos\theta \frac{\phi(3 - \phi^2)}{4} + \frac{\sigma_{w1} + \sigma_{w2}}{2}, \tag{2.7}$$

in which θ is the static contact angle as illustrated in figure 1, measured inside the shell fluid 1; σ_{w1} and σ_{w2} are respectively the wall energies associated with fluids 1 and 2, and are related to the contact angle through Young's equation $\sigma_{w2} - \sigma_{w1} = \sigma \cos\theta$; they do not really enter the boundary conditions because of the derivative in (2.6). Note that the advancing and the receding contact angles are the same as the static one and the contact angle hysteresis is not accounted for in this formalism. By allowing relaxation of the wall energy, the diffuse-interface theory can accommodate a dynamic contact angle that deviates from the static one (Yue & Feng 2011). Contact angle hysteresis is a much more complex issue, and existing models are mostly *ad hoc*. Thus, we have decided to exclude it in the present study.

https://doi.org/10.1017/jfm.2011.235 Published online by Cambridge University Press

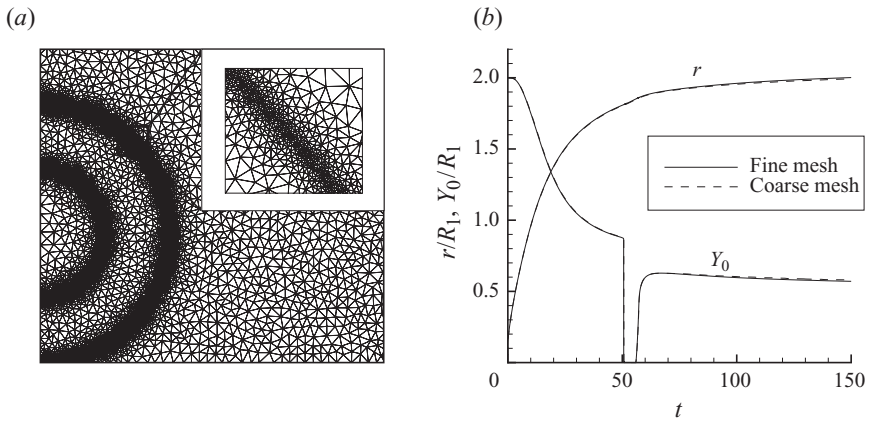


FIGURE 2. (*a*) A representative mesh with adaptive refinement. The inset shows details of the interface. (*b*) Mesh convergence test in terms of r (radius of the contact area) and Y_0 (height of the outer drop). Initially, the fine and coarse meshes have 4.8×10^4 and 2.2×10^4 elements, respectively. $R_2/R_1 = 0.5$, $\theta = 30^\circ$ and $\mu_2/\mu_1 = 1$. Time is scaled by $\mu_1 R_1/\sigma$ and the same dimensionless time is used in the following figures.

With inertia and gravity neglected, the problem is governed by five dimensionless numbers: the contact angle θ, the radius ratio R_2/R_1, the viscosity ratio μ_2/μ_1, the Cahn number $Cn = \epsilon/R_1$ and $S = \sqrt{\gamma\mu^*}/R_1$ with $\mu^* = \sqrt{\mu_1\mu_2}$. Here, Cn, the dimensionless interfacial thickness, should be small enough to approach the sharp-interface limit (Zhou, Yue & Feng 2010). S is the dimensionless diffusion length, which is a counterpart of the slip length commonly used in sharp-interface models to avoid the stress singularity at the contact line (Cox 1986; Yue *et al.* 2010). In our formulation of the diffuse-interface method, the movement of the contact line is solely driven by the Cahn–Hilliard diffusion across the interface. The following results were obtained using $Cn = 0.005$ and $S = 0.005$ such that both the interfacial thickness and the diffusion length are much smaller than the characteristic length of the flow, and the sharp-interface limit is attained (Yue *et al.* 2010).

The governing equations together with the boundary conditions are solved using a finite-element package AMPHI (Yue *et al.* 2006*b*), which employs triangular elements and adaptive meshing. The latter is crucial for capturing the steep variation of ϕ across the interface; it allows us to compute a very thin interface at manageable cost. A typical mesh is illustrated in figure 2(*a*). In this case, the finest mesh size at the interface is approximately 0.5ϵ. Time stepping is via a second-order fully implicit scheme. Details of the numerical method and its validation are described by Yue *et al.* (2006*b*) and Zhou *et al.* (2010). In particular, Zhou *et al.* (2010) performed simulations of the spreading of a simple drop and obtained satisfactory agreement with the numerical simulations of Khatavkar, Anderson & Meijer (2007) and the experiments of Zosel (1993). In the current study, we have also performed mesh convergence tests. Figure 2(*b*) shows the time history of the radius r of the contact area (see figure 1*b*) and the height of the outer drop Y_0 computed using a coarse mesh and a fine one, the latter having more than twice as many elements. These computations correspond to the conditions of figure 6, and the sudden dip and rise of Y_0 indicate the rupture of the shell and the subsequent appearance of the sessile drop. The solid and dashed curves can hardly be distinguished and thus the numerical results are mesh-independent.

https://doi.org/10.1017/jfm.2011.235 Published online by Cambridge University Press

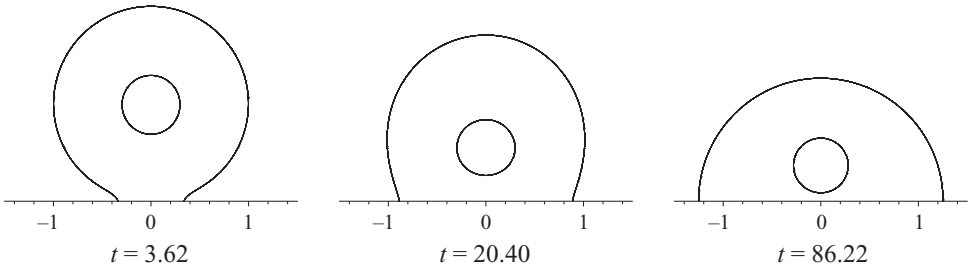


FIGURE 3. Time sequence of the drop morphology during spreading in regime I at $R_2/R_1 = 0.3$, $\theta = 90^\circ$ and $\mu_2/\mu_1 = 1$. The core is always suspended above the substrate.

3. Results

Based on simple geometric and physical arguments, one can anticipate three possible flow regimes for spreading of the compound drop (figure 1). First, when R_2 is small, the inner drop may never touch the substrate. This spreading process is sketched in figure 1(b,c) and denoted as regime I. As R_2 increases, the inner drop is pushed towards the substrate by the downward flow due to spreading, and eventually becomes attached to it (figure 1d,e). This process will be called regime II. A further increase in R_2 leads to regime III, in which the compound drop breaks up as shown in figure 1(f,g). Depending on the wetting property of the substrate, the breakup can be triggered either by the coalescence between the apexes of the two fluid–fluid interfaces (figure 1f) or by the merging of the contact lines (figure 1g). We will show below that these scenarios do not constitute the whole picture. The dynamics of interfacial deformation and transient flow gives rise to more complex interfacial morphologies. In particular, we have found two sub-regimes in regime II and three sub-regimes in regime III. For brevity, we will refer to the inner drop as the 'core', and the outer drop simply as the 'drop'. Terms such as contact angle and wettability refer to those of the shell (fluid 1).

3.1. *Flow regimes*

3.1.1. *Regime I: suspended core*

Regime I occurs for a small core, a large contact angle, or both. A typical time sequence of the drop morphology is illustrated in figure 3 for $R_2/R_1 = 0.3$, $\theta = 90^\circ$ and $\mu_2/\mu_1 = 1$. In this and most subsequent plots of temporal evolution, the final frame shows the steady equilibrium configuration. Although the core is pushed downwards by the spreading flow, this effect is not strong enough to induce contact between the core and the substrate. Therefore, the core remains encapsulated inside the drop and there is only one contact line in the equilibrium state. Typically, the core sustains little deformation during the spreading and remains more or less spherical. This is owing to the small core size and slow spreading of the shell fluid (with a large θ), which conspire to produce a small capillary number for the inner drop.

3.1.2. *Regime II: sessile core*

With a larger core, the spreading flow causes the core to make eventual contact with the substrate, as shown in figure 4 for $R_2/R_1 = 0.6$ with the other parameters being the same as in figure 3. This contact or wetting of the substrate by the core will be juxtaposed with the rupture of the shell in later regimes, and for convenience will be called *coalescence* henceforth, even though the term usually refers to the joining of two domains of the same substance.

https://doi.org/10.1017/jfm.2011.235 Published online by Cambridge University Press

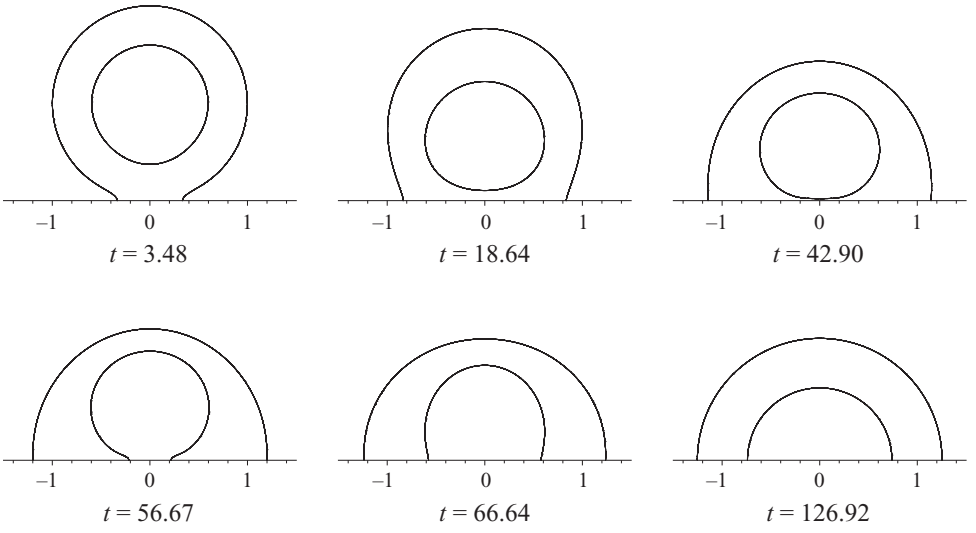


FIGURE 4. Time sequence of the drop morphology during spreading in regime II_1 at $R_2/R_1 = 0.6$, $\theta = 90^\circ$ and $\mu_2/\mu_1 = 1$. The core comes into contact with the substrate and is attached to it in the final equilibrium state.

Before coalescence, the core is deformed into an oblate shape by the flow in the spreading shell and pressed against the substrate. In this case, the coalescence occurs at the centre of the contact area, which then expands into a new contact line. Thus, the dynamics in this regime, denoted as regime II_1, consists of two spreading processes, one associated with the outer interface and the other with the inner interface. Eventually, both interfaces adjust themselves to form an equilibrium compound drop characterized by a sessile core. In this case, the substrate area wetted by the shell fluid is a ring rather than a circle as in regime I. Since a neutrally wetting substrate ($\theta = 90^\circ$) is used here, the two interfaces are concentric, which is generally not the case (see figure 1*d*, *e*).

A further increase of the core size leads to regime II_2 with the additional feature of droplet entrapment on the substrate. Figure 5 shows the drop morphology for $R_2/R_1 = 0.9$, $\theta = 90^\circ$ and $\mu_2/\mu_1 = 1$. The large core is easily deformed by the spreading-driven flow, and it approaches the substrate with a somewhat flat bottom, below which a thin film of the shell fluid develops. The pressure within the film is high owing to the lubrication effect and it slows down the descending of the core. The drainage in the film is associated with a radial pressure gradient, which pushes the core inward to form a dimple. This is similar to that formed between two coalescing drops (Yue *et al.* 2005) and on the inner side of a torus contracting onto itself (Yue *et al.* 2006*b*). Thus, the lubricating film first ruptures along a circle rather than at the centre point ($t = 59.77$ in figure 5). This generates two new contact lines, with a small amount of the shell fluid entrapped inside the core. In time it shrinks into a much smaller sessile drop. The final morphology is a sessile 'triple compound drop', with a shell of fluid 1 enclosing the core of fluid 2, which in turn encapsulates a daughter drop of fluid 1.

3.1.3. *Regime III: drop breakup*

When the core is very large, or when the contact angle is far from 90°, the shell breaks up and releases the core into the ambient fluid. The rupture may occur at the

https://doi.org/10.1017/jfm.2011.235 Published online by Cambridge University Press

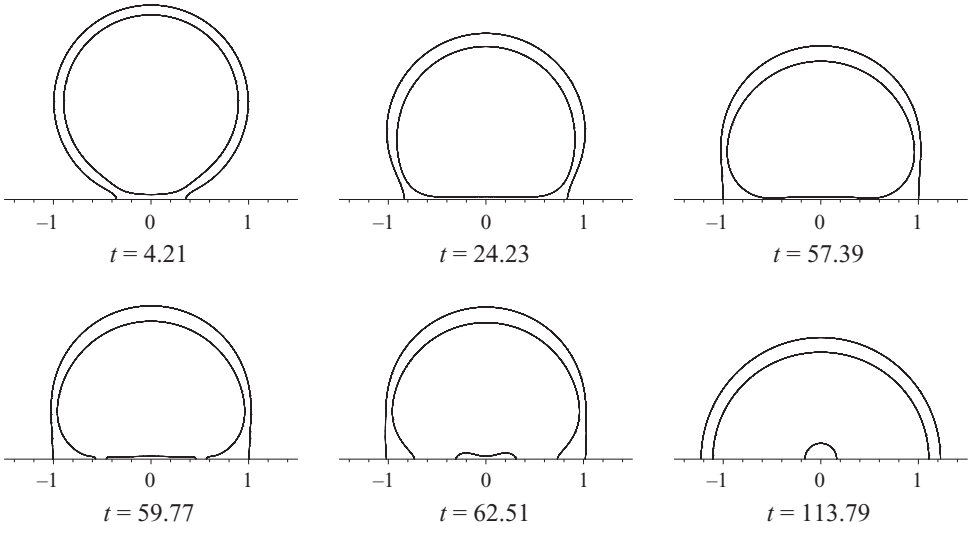


FIGURE 5. Time sequence of the drop morphology during spreading in regime II_2 at $R_2/R_1 = 0.9$, $\theta = 90^\circ$ and $\mu_2/\mu_1 = 1$. The coalescence between the core and the substrate onsets off-centre along a circle, resulting in a sessile daughter droplet residing inside the core.

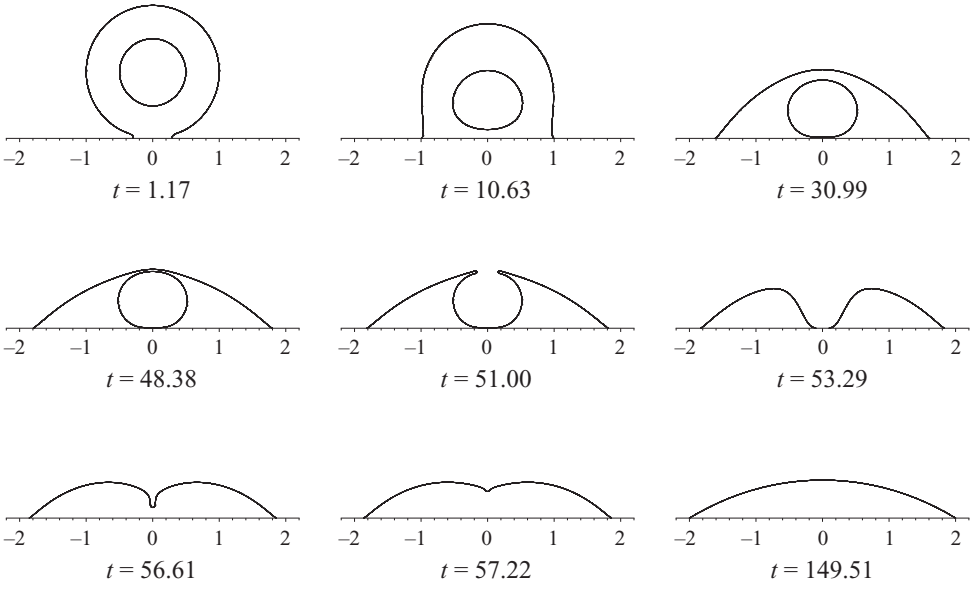


FIGURE 6. Time sequence of the drop morphology during spreading in regime III_1 at $R_2/R_1 = 0.5$, $\theta = 30^\circ$ and $\mu_2/\mu_1 = 1$. The rupture of the shell occurs at the apex of the drop and a simple sessile drop is formed after the breakup.

apex of the drop, on its side or at the contact line, corresponding to three sub-regimes III_i $(i = 1, 2, 3)$ respectively.

A typical illustration of regime III_1 is shown in figure 6 for $R_2/R_1 = 0.5$, $\theta = 30^\circ$ and $\mu_2/\mu_1 = 1$. The spreading behaviour and the deformation of the core in the early stage are similar to figure 4. However, the contact angle is small and the shell fluid spreads rapidly, causing the outer interface to press on the relatively large core. Then

https://doi.org/10.1017/jfm.2011.235 Published online by Cambridge University Press

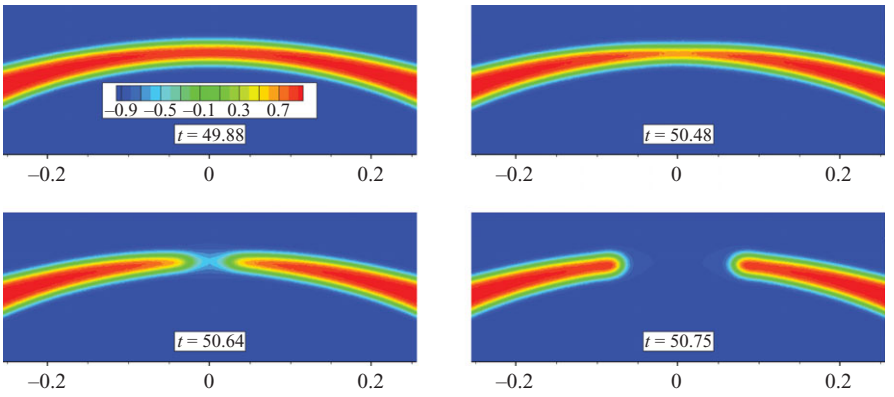


FIGURE 7. (Colour online available at journals.cambridge.org/FLM) Details of the rupture of the shell depicted by ϕ contours during the process shown in figure 6. The edges of the shell correspond roughly to $\phi = -0.9$.

the thin film at the top of the drop ruptures; a hole nucleates and rapidly expands ($t = 51$). Shortly after, the core also coalesces with the substrate ($t = 53.29$), generating a configuration with a ring of the shell fluid surrounding a 'dry' (with the ambient fluid) central region. For other parameters, we have also observed the coalescence with the substrate occurring before the rupture of the shell. Finally, the ring contracts to form a simple sessile drop. At higher contact angles, a small amount of the ambient fluid can be trapped inside to produce a sessile compound drop in the end.

The rupture of the shell between $t = 48.38$ and 51 warrants a closer inspection (figure 7). In sharp-interface models, such singular topological changes cannot be computed but are effected by *ad hoc* means. In diffuse-interface models, in contrast, they occur spontaneously and smoothly. The singularity has been regularized by the diffuseness of the interface; rupture occurs through the evolution of the continuous phase field ϕ. Moreover, the diffuse-interface model includes short-range interaction between interfaces akin to van der Waals forces (Feng *et al.* 2005). In figure 7, the shell thins until its thickness approaches the interfacial thickness ($t = 50.48$). Then the short-range attraction between the interfaces acts to fuse them into one ($t = 50.64$), which subsequently breaks and pulls back to form a hole ($t = 50.75$). All breakup processes to be discussed hereafter have essentially the same diffuse-interface mechanism.

Figure 8 shows a typical case of regime III_2 for $R_2/R_1 = 0.8$, $\theta = 30^\circ$ and $\mu_2/\mu_1 = 1$. The core is larger and the swift spreading of the shell fluid causes such a strong flow as to squash the core significantly. A film forms between the core and the substrate during the spreading as in figure 5. More importantly, the transverse extension of the core creates a 'shoulder' where the shell thickness is minimum ($t = 89.23$). Further spreading leads to the rupture of the shell. Thus, different from regime III_1, the shell disintegrates with the top cap breaking off rather than a hole puncturing the top. This gives rise to a configuration with a circular cap on top of a base ($t = 94.10$). Eventually, the cap retracts to form a suspended daughter drop, and the shell fluid in contact with the substrate shrinks to a sessile drop. In the sequence shown, the core is always insulated from the substrate by a thin film of fluid 1. However, it can also coalesce with the substrate at larger radius ratios, e.g. $R_2/R_1 = 0.9$. When this happens, a droplet of fluid 1 is sometimes entrapped in the centre, similar to figure 5. In the end, the ring of fluid 1 contracts onto the central droplet to form a sessile drop.

https://doi.org/10.1017/jfm.2011.235 Published online by Cambridge University Press

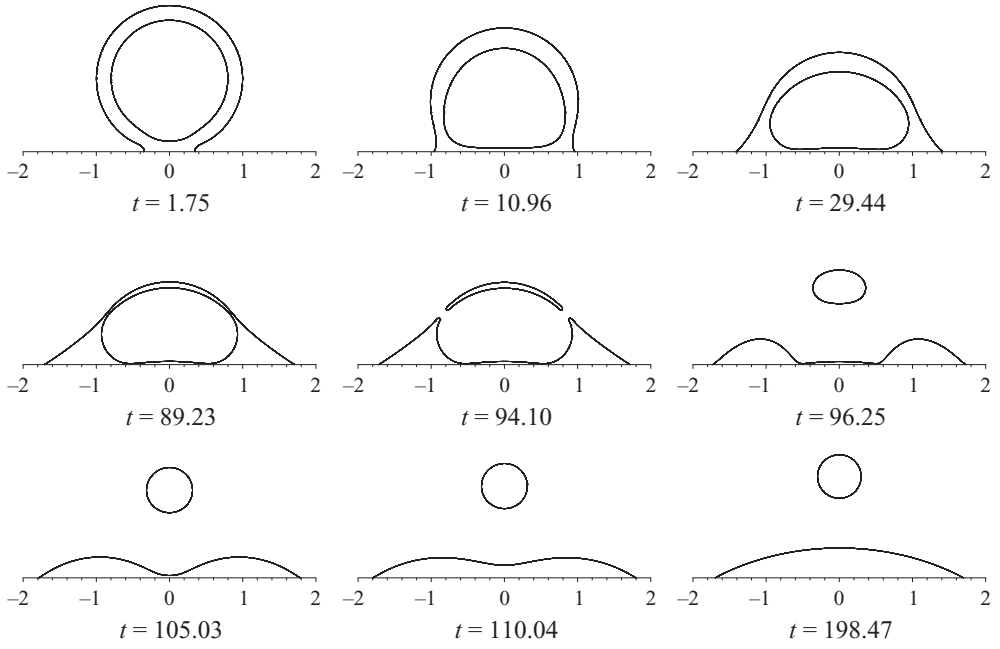


FIGURE 8. Time sequence of the drop morphology during spreading in regime III_2 at $R_2/R_1 = 0.8$, $\theta = 30^\circ$ and $\mu_2/\mu_1 = 1$. The rupture of the shell occurs on the shoulder of the drop, producing a suspended daughter drop and a sessile drop.

As a special case of regime III_2, we show the breakup of the compound drop with a very thin shell in figure 9 for $R_2/R_1 = 0.95$, $\theta = 30^\circ$ and $\mu_2/\mu_1 = 1$. This might provide insight into the rupture of a soap bubble when touching a solid wall. The spreading of the shell fluid is such that the thinnest point is just above the contact line. There, the shell ruptures at an early stage of the spreading, producing a suspended fluid 'parachute' and a pancake-shaped thin film attached to the substrate. Both structures retract in time to form a suspended drop and a sessile drop, with the former much larger than the latter. The retraction of the film is much slower than that of the shell, because the well-wetted substrate provides considerable friction against the receding of the contact line. Also note that the parachute develops a rim during the retraction ($t = 5.34$), a process commonly detected in the rupture of soap films and bubbles and attributed to inertia (Ranz 1959; Taylor 1959; Culick 1960). In our simulation, inertia is absent. Rather, the appearance of the rim is thanks to the viscosity of the ambient fluid, which should have been negligible for air in soap bubble experiments. As the shell retracts, the viscous shear at the interface drives the shell fluid towards the edge, resulting in a rim. We have performed calculations using a lower viscosity ratio $\mu_2/\mu_1 = 0.1$, and the rim is much less prominent.

Finally, we show a distinct breakup scenario, i.e. regime III_3, which occurs when the contact angle is high and the core is relatively large. Figure 10 illustrates a typical case for $R_2/R_1 = 0.7$, $\theta = 120^\circ$ and $\mu_2/\mu_1 = 1$. The early stage of the spreading is similar to regime II with the core moving downwards and coalescing with the substrate ($t \leqslant 83.04$). Since the substrate is non-wettable to the shell fluid, the core tends to spread over it, with the inner contact line advancing much faster than the outer one. The two contact lines become closer and eventually merge ($t = 97.9$). Then the shell fluid immediately detaches from the substrate and forms a simple suspended drop. A

https://doi.org/10.1017/jfm.2011.235 Published online by Cambridge University Press

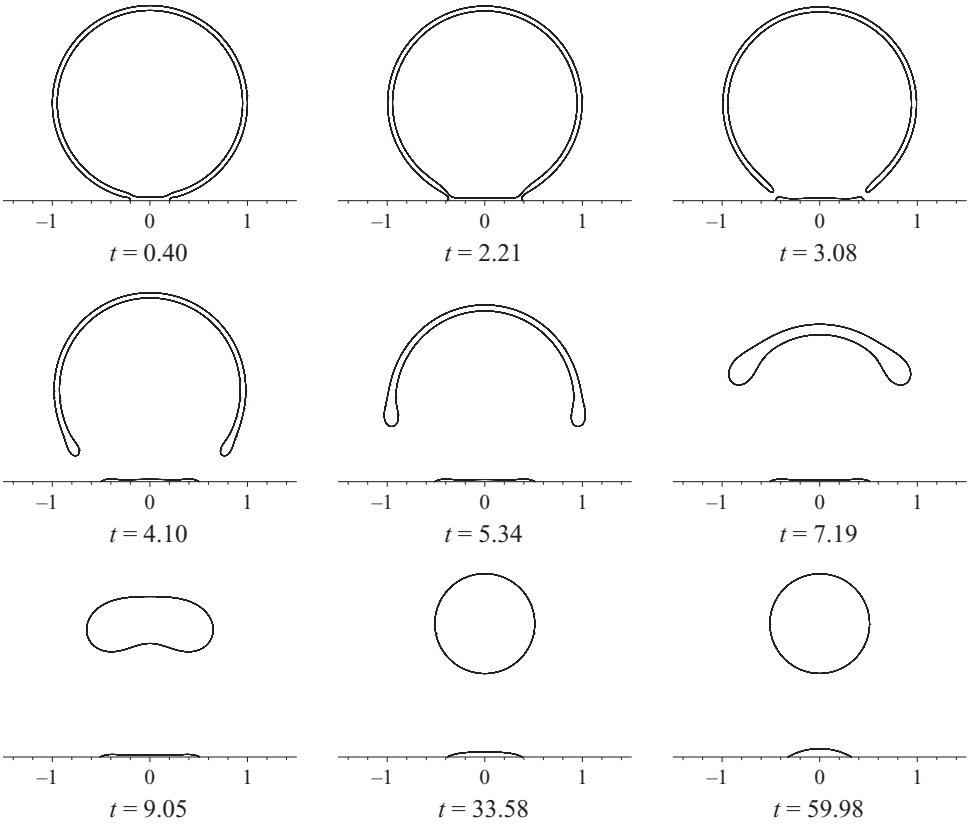


FIGURE 9. Time sequence of the drop morphology during spreading in regime III_2 at $R_2/R_1 = 0.95$, $\theta = 30^\circ$ and $\mu_2/\mu_1 = 1$. The shell ruptures just above the contact line to produce a parachute of fluid 1, which contracts into a suspended daughter drop much larger than the sessile drop.

slightly different final morphology may appear for larger radius ratios, when a small amount of the shell fluid is trapped in the core after its coalescence with the substrate, as in figure 5. In this case, a tiny sessile drop will remain below the suspended one in the end.

3.2. *Phase diagram*

Now we can summarize the regimes described so far in a 'phase diagram' in the parameter space. First, some geometric considerations provide a guideline for the boundaries of regimes I and II (cf. figure 1). In the absence of external forces such as gravity, all the interfaces should be spherical in equilibrium. For regime I, the diameter of the core should be less than the height of the compound drop. For regime II, the height of the core should be less than that of the whole drop when $\theta < 90^\circ$ (figure 1*d*), and the diameter of the inner contact line should be less than that of the outer contact line when $\theta > 90^\circ$ (figure 1*e*). Together with the mass conservation conditions of the shell and the core, these constraints give the upper limits of the radius ratio

$$\frac{R_2}{R_1} < R_c^I(\theta) \equiv \left[\frac{1-\cos\theta}{4+2\cos\theta}\right]^{1/3}, \tag{3.1}$$

https://doi.org/10.1017/jfm.2011.235 Published online by Cambridge University Press

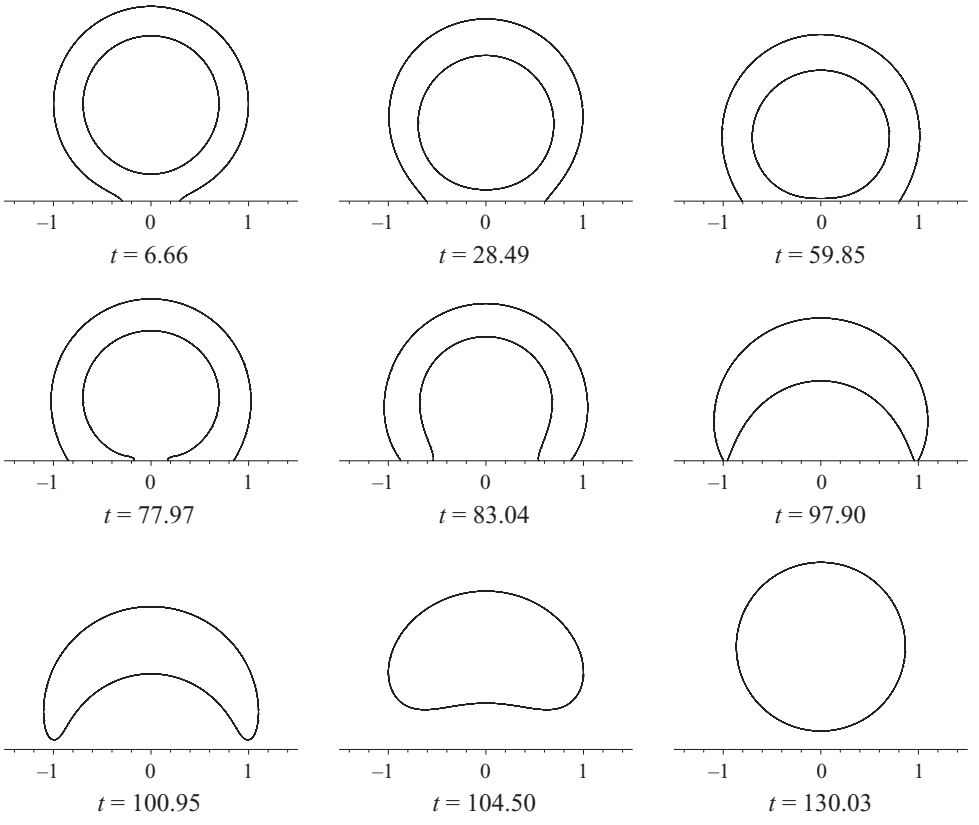


FIGURE 10. Time sequence of the drop morphology during spreading in regime III_3 at $R_2/R_1 = 0.7$, $\theta = 120^\circ$ and $\mu_2/\mu_1 = 1$. The breakup is triggered by the merging of the contact lines and the fluid shell evolves into a simple drop suspended in the ambient fluid.

$$\frac{R_2}{R_1} < R_c^{II}(\theta) \equiv \left[\frac{2-\cos\theta}{2+\cos\theta}\min\left(\tan^2\tfrac{1}{2}\theta, \cot^4\tfrac{1}{2}\theta\right)\right]^{1/3}, \tag{3.2}$$

for regimes I and II, respectively. Since the dynamic process is not accounted for in obtaining these formulae, they represent critical conditions for an imaginary quasi-static spreading process. In practice, they serve as necessary but insufficient conditions for the occurrence of these equilibrium states.

We have performed a parametric study of the spreading and breakup behaviour for various values of R_2/R_1 and θ, and constructed a phase diagram of the flow regimes in figure 11 for a fixed viscosity ratio $\mu_2/\mu_1 = 1$. The effect of the viscosity ratio will be discussed at the end of this subsection. The geometric constraints (3.1) and (3.2) are also shown by the solid curves for comparison with the real boundaries between the flow regimes. Note first that the upper boundary of regime I is well below the geometric constraint (3.1). With increasing radius ratio, transitions from regime I to the other regimes occur by the core coalescing with the substrate. The final fate of the compound drop depends on the contact angle. For $\theta < 120^\circ$, a stable equilibrium state with a sessile core prevails (regime II_1). For $\theta > 120^\circ$, the compound drop breaks up (regime III_3). In the dynamic process, the effect of the flow is mostly to move the inner drop towards the substrate. Thus, a core with a radius ratio less than R_c^I can make contact with the substrate. This renders the real boundary of regime I well

https://doi.org/10.1017/jfm.2011.235 Published online by Cambridge University Press

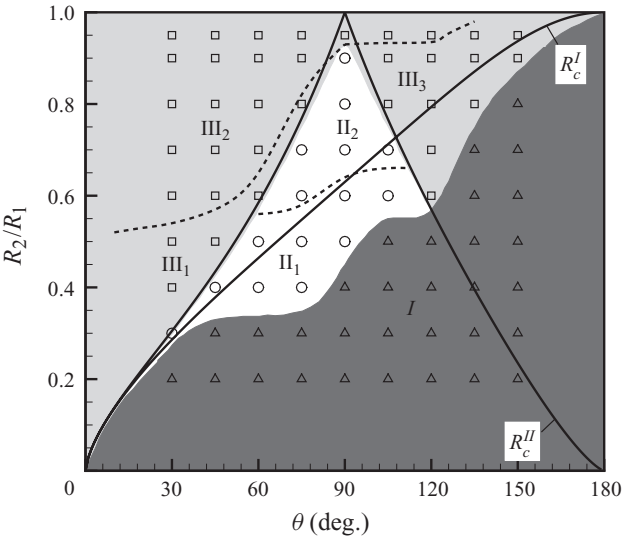


FIGURE 11. Phase diagram in the (θ, R_2/R_1)-plane representing the three flow regimes for $\mu_2/\mu_1 = 1$. Regimes I (triangles), II (circles) and III (squares) are also distinguished by different grey scales. The sub-regimes are delineated by the dashed curves. The boundaries among regimes and sub-regimes are approximate and serve as a guide to the eye. The geometric constraints for regimes I and II, according to (3.1) and (3.2) respectively, are plotted by the solid curves for reference.

below the curve of (3.1). In contrast, the real boundary between regimes II and III is very close to the curve of R_c^{II} in (3.2). Here the dominant effect is the spreading of the fluids on the substrate rather than the flow in the shell. The latter does not introduce new breakup mechanisms beyond the coalescence and subsequent spreading of the core illustrated in figures 6 and 10. Thus, the transition between regimes II and III is insensitive to the transient flow. A small discrepancy may arise from the entrapment of a droplet inside the core (cf. figure 5), which effectively increases the core size and thus shifts the upper boundary of regime II slightly below R_c^{II}, as exhibited in figure 11. This effect is very weak since the volume of the trapped drop is always small.

The phase diagram in figure 11 is for equal viscosity of the two components: $\mu_1 = \mu_2$, and we will now discuss the effect of a viscosity contrast. As discussed above, the transition from regime II to III is primarily determined by the geometric constraint (3.2) rather than the transient flow. Thus, the viscosity ratio has a negligible influence on the upper boundary of regime II since (3.2) is independent of the viscosity. In addition, the breakup scenarios within different regimes are found to be qualitatively similar for different viscosity ratios; the most prominent effect of the viscosity ratio is to modify the contact line speed and hence the time scale of the spreading process.

The only qualitatively important effect of the viscosity ratio concerns the boundary between regimes I and II. At $R_2/R_1 = 0.5$ and $\theta = 90^\circ$, which lies just above the I–II boundary in figure 11, we computed two additional viscosity ratios $\mu_2/\mu_1 = 0.1$ and 10. While the final state remains in regime II for the higher viscosity ratio, it falls into regime I for the lower viscosity ratio. Therefore, a lower viscosity ratio (i.e. less viscous core and ambient fluid) tends to hinder the coalescence between the core and the substrate and raise the upper boundary of regime I. Two factors may potentially be at play. A more viscous core will respond better to the surrounding flow, and thus

https://doi.org/10.1017/jfm.2011.235 Published online by Cambridge University Press

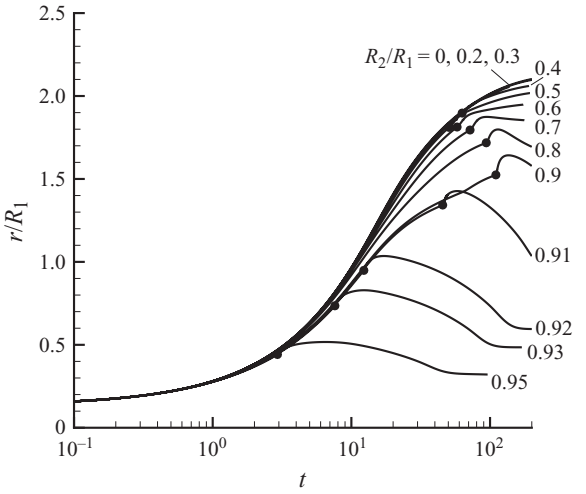


FIGURE 12. Spreading of compound drops with various R_2/R_1 in terms of the temporal evolution of the radius of the outer contact line $r(t)$ for $\mu_2/\mu_1 = 1$ and $\theta = 30^\circ$. The filled circles on curves with $R_2/R_1 \geqslant 0.4$ mark the point of rupture of the shell in regime III.

move more readily toward the substrate. Besides, it will be less able to deform and flatten its lower surface, thereby allowing more rapid draining of the shell fluid in the lubricating film.

3.3. *Temporal evolution*

So far we have focused on the equilibrium configuration of the interface after breakup. Now we examine the transient process of spreading and breakup more quantitatively. For a series of radius ratios, figure 12 depicts the spread of the compound drop on a hydrophilic substrate in terms of the contact line radius $r(t)$ (see figure 1*b*). The spread of a simple drop ($R_2/R_1 = 0$) is also shown for comparison. The range of R_2/R_1 covers transitions between regimes I, II_1, III_1 and III_2 in that order. For all core sizes, the early stage of the spreading (say $t < 3$) is insensitive to the presence of the core. This is not surprising since the spreading is determined by the competition between interfacial tension and viscous force at the contact line. The presence of the core has yet to be felt. For the smallest core sizes, $R_2/R_1 = 0.2$ and 0.3, this is true for the entire duration of the spreading; these curves, corresponding respectively to regimes I and II, can hardly be distinguished from that of the simple drop. For $R_2/R_1 \geqslant 0.4$ (regime III), the compound drop ruptures at the point marked by the solid circle on each curve. Before the rupture, the spreading is hindered for larger core sizes. The rupture causes a sudden acceleration of the spreading as the hindrance due to the core disappears. For $R_2/R_1 \geqslant 0.7$, r eventually decreases, corresponding to the retraction of the disk or ring of the shell fluid after the generation of a suspended daughter drop (figure 8).

A similar analysis has been done for a hydrophobic substrate, where increasing R_2/R_1 leads to transition from regime I to III_3. The main features are similar. In regime III_3, the coalescence of the core on the substrate induces a sharp upturn in the spreading curve resembling that in figure 12 due to the rupture of the shell. The curves end at the merging of the contact line and the detachment of the drop from the substrate.

https://doi.org/10.1017/jfm.2011.235 Published online by Cambridge University Press

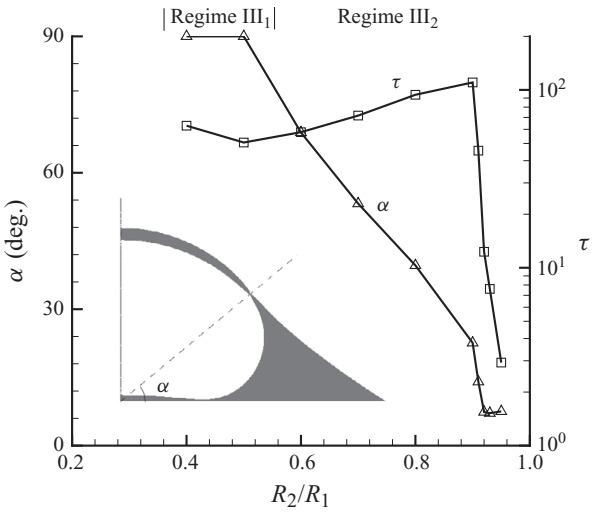


FIGURE 13. Time and location of film rupture in regime III as functions of the radius ratio R_2/R_1 for $\mu_2/\mu_1 = 1$ and $\theta = 30°$. The polar angle α of the rupture point is illustrated in the inset.

In regime III, the time and location of the rupture of the shell show a strong and intriguing dependence on R_2/R_1 (figure 13). For relatively small core sizes in regime III_1 (say $R_2/R_1 = 0.4$ and 0.5), the rupture occurs at the apex ($\alpha = 90°$). With increasing core size, the pinch-off point shifts down the shoulder; α decreases to roughly 7° at $R_2/R_1 = 0.92$ and then levels off. Now the rupture happens very close to the contact line where the interfaces are distorted (cf. figure 9). With further increase of R_2/R_1, the point of rupture shifts radially inward, with little further change in α.

The time interval τ, from the start to the rupture, can be considered the lifetime of the compound drop, and it exhibits a highly non-monotonic dependence on R_2/R_1. First, it decreases with R_2/R_1 in regime III_1, since the coalescence between the apexes of the core and the compound drop occurs more readily for a larger core. In regime III_2 ($R_2/R_1 > 0.5$), τ rises with the radius ratio till $R_2/R_1 = 0.9$ and then drops precipitously. The rise is owing to the slower drainage as the shell becomes thinner (Rushton & Davies 1983). The sharp decline is due to a change in the mechanism of rupture. For such large core sizes, the rupture is triggered by the bending of the meniscus near the contact line rather than the drainage of the shell fluid (see figure 9). Overall, a compound drop with $R_2/R_1 = 0.9$ survives the longest.

We should point out a limitation of the diffuse-interface model in simulating breakup. The exact time of the interfacial rupture depends to a degree on the interfacial thickness ϵ. Although we have reached the sharp-interface limit at the contact line as defined by Yue *et al.* (2010), the breakup features a length scale that continually decreases in time, eventually approaching the thickness of the interface. The simulation beyond this point is subject to a finite-ϵ effect of accelerated pinch-off relative to reality. For partial coalescence between a drop and an interface, Yue, Zhou & Feng (2006*a*) showed that this amounts to an underestimation of the pinch-off time in comparison with experiment. Numerical experimentation here, with Cn decreasing from 0.02 to 0.0025, bears out the same conclusion: the rupture of the film is delayed for thinner interfaces. The smallest length scale to be resolved being ϵ, the magnitude of the computation is determined by R_1/ϵ. Thus, for larger drops,

https://doi.org/10.1017/jfm.2011.235 Published online by Cambridge University Press

we expect a more serious underestimation of the pinch-off time because the diffuse interface may be much thicker than the real one. For micron-sized drops, which are of interest here, we can resolve interfaces down to 10 nm thick, comparable with real interfaces. In this case, the pinch-off time should be close to the real one as the finite ϵ reflects reality. Of course, the challenge to resolve small length scales during morphological changes exists for all continuum simulation methods. Among these, the diffuse-interface method probably handles the challenge most successfully.

3.4. *Inertial effects*

So far we have neglected inertia. This is justifiable for small or highly viscous drops. Take the simulation of figure 6 for example. Transient capillary and Weber numbers can be estimated from the velocity U of film retraction just after rupture ($t = 51$): $Ca = \mu_1 U/\sigma = 0.34$ and $We = \rho_1 U^2 h/\sigma = 0.12$, where we have taken $\mu_1 = 10^{-3}$ Pa s and $\rho_1 = 10^3$ kg m^{-3} to be the viscosity and density of water, $\sigma = 20$ dyn cm^{-1} to be a typical interfacial tension, say between water and olive oil, and the thickness of the film $h = 0.05R_1$ for an initial drop radius $R_1 = 1$ μm. In this case, therefore, inertia plays a secondary role to capillarity. For the more viscous silicone oils used by Debrégeas, Martin & Brochard-Wyart (1995) and Debrégeas, de Gennes & Brochard-Wyart (1998), $We \ll 1$ and inertia can be safely neglected.

For soap films rupturing in air, on the other hand, inertia can be important (see e.g. Culick 1960; Savva & Bush 2009). To elucidate the potential role of inertia in the compound-drop breakup discussed here, we have repeated some of the simulations using the full Navier–Stokes equations. Two new dimensionless numbers are introduced: the Ohnesorge number $Oh = \mu_1/\sqrt{\rho_1 \sigma R_1}$ and the density ratio ρ_2/ρ_1, with ρ_1 and ρ_2 being the density of fluids 1 and 2, respectively. Oh represents the relative importance of viscous forces with respect to inertial–capillary forces; a smaller Oh corresponds to a compound drop with a smaller viscosity or larger radius. We have tested $Oh = 0.224$ and 0.0707 for the conditions of figure 9. The viscosity and density of the two fluids are matched for simplicity.

For $Oh = 0.224$, the evolution of the drop morphology is essentially the same as in figure 9, consistent with the small Ca and We estimated above. The only difference is that the breakup is slightly delayed by inertia and the suspended drop oscillates once before equilibrium. At $Oh = 0.0707$, inertia becomes more important and qualitative differences are observed. Figure 14 shows that the early stages of the spreading and breakup are similar to figure 9, except that the process is much slower. Later, the retraction of the shell produces a much more pronounced rim ($t = 11.99$ and 17.97), characteristic of films retracting with large inertia (Ranz 1959; Savva & Bush 2009). The rim then closes in onto the axis and traps some ambient fluid, generating a suspended compound drop as opposed to the single drop of figure 9.

For compound drops with a larger radius or smaller viscosity, hence an even smaller Oh, inertia may lead to new flow regimes and breakup scenarios beyond those discussed above. As the focus of this paper is on inertialess dynamics of compound-drop spreading, we leave a comprehensive investigation of inertial effects to a future endeavour.

4. Conclusions

We have performed numerical simulations of the spreading and breakup of W/O/W-type compound drops on a solid substrate. A diffuse-interface method is used to deal with the moving contact line and the topological change of the drop

https://doi.org/10.1017/jfm.2011.235 Published online by Cambridge University Press

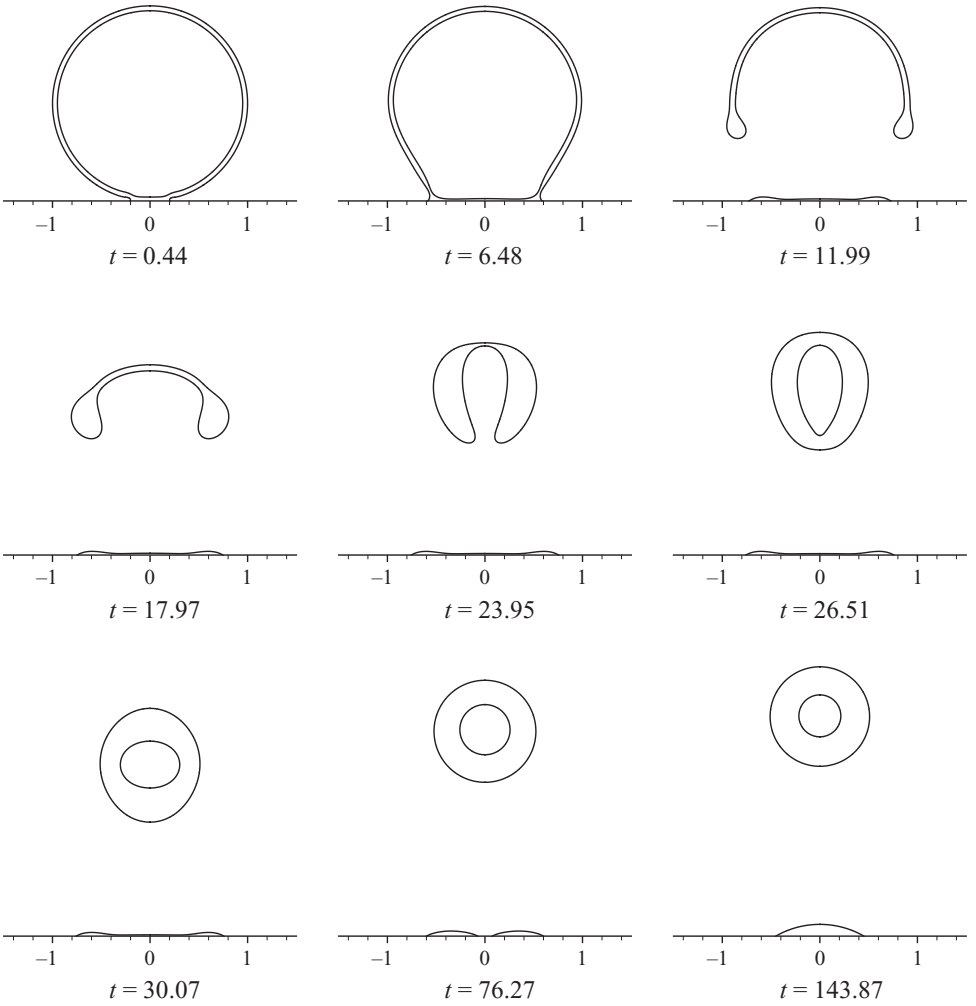


FIGURE 14. Inertial effects on the spreading and rupture of a compound drop at $Oh = 0.0707$ and $\rho_2/\rho_1 = 1$. Other parameters are the same as in figure 9.

morphology. With negligible inertia and gravity, we have observed three regimes for the interfacial behaviour.

(*a*) When the core is small or the substrate is hydrophobic to the shell fluid, the core remains encapsulated in the shell, and the spreading behaviour is similar to that of a simple drop.

(*b*) A moderately large core can wet the substrate without destroying the integrity of the compound drop, with a final configuration of a sessile core inside the shell. This regime is inhibited if the substrate is highly hydrophobic to the shell fluid.

(*c*) The compound drop breaks up spontaneously when the core is sufficiently large. This is facilitated by a substrate that is either highly hydrophilic or moderately hydrophobic to the shell fluid. In the former case, the shell ruptures at a location that shifts from the apex towards the substrate with increasing core size. In the latter, the breakup is typically triggered by merging of contact lines on the substrate. In order to avoid drop breakup, a neutrally wetting substrate is preferred.

https://doi.org/10.1017/jfm.2011.235 Published online by Cambridge University Press

In some of these scenarios, considerable deformation of the core leads to the formation of secondary drops of the shell fluid, either entrapped inside the core and attached to the substrate or freely suspended in the ambient fluid. In an application, these secondary drops corrupt the monodispersity of the double emulsion and may be undesirable. Viscosity of either fluid component tends to slow down the spreading process. However, the breakup scenarios and final interfacial morphology are insensitive to the viscosity ratio between the two fluids.

Since the spreading of compound drops on substrates has received little attention in prior research, the value of this work lies in the discovery of these complex and intriguing scenarios of interfacial evolution. The theoretical model and numerical method have been carefully validated in the past and applied successfully to a host of interfacial flow simulations. Nevertheless, the flow regimes described in this study remain to be confirmed by experiments. We have focused on micron-sized drops with negligible inertial and gravitational effects. Larger compound drops will likely exhibit additional dynamics due to one of these factors. Thus, much remains to be researched in this area.

We acknowledge support by the Petroleum Research Fund, the Canada Research Chair programme, NSERC (Discovery, Accelerator and Strategic grants) and the Canada Foundation for Innovation. P.G. also acknowledges funding by the Fundamental Research Funds for the Central Universities (USTC) and the Special Foundation of the President of the Chinese Academy of Sciences. The computations were done on WestGrid.

REFERENCES

Bird, J. C., de Ruiter, R., Courbin, L. & Stone, H. A. 2010 Daughter bubble cascades produced by folding of ruptured thin films. *Nature* **465**, 759–762.

Bonn, D., Eggers, J., Indekeu, J., Meunier, J. & Rolley, E. 2009 Wetting and spreading. *Rev. Mod. Phys.* **81**, 739–805.

Chiu, S. L. & Lin, T. H. 2005 Experiment on the dynamics of a compound drop impinging on a hot surface. *Phys. Fluids* **17**, 122103.

Cox, R. G. 1986 The dynamics of the spreading of liquids on a solid surface. Part 1. Viscous flow. *J. Fluid Mech.* **168**, 169–194.

Culick, F. E. C. 1960 Comments on a ruptured soap film. *J. Appl. Phys.* **31**, 1128–1129.

Debrégeas, G., de Gennes, P. G. & Brochard-Wyart, F. 1998 The life and death of 'bare' viscous bubbles. *Science* **279**, 1704–1707.

Debrégeas, G., Martin, P. & Brochard-Wyart, F. 1995 Viscous bursting of suspended films. *Phys. Rev. Lett.* **75**, 3886–3889.

Engel, R. H., Riggi, S. J. & Fahrenba, M. J. 1968 Insulin: Intestinal absorption as water-in-oil-in-water emulsions. *Nature* **219**, 856–857.

Feng, J. J., Liu, C., Shen, R. & Yue, P. T. 2005 An energetic variational formulation with phase field methods for interfacial dynamics of complex fluids: Advantages and challenges. In *Modeling of Soft Matter* (ed. M.-C. T. Calderer & E. Terentjev), IMA Volumes in Mathematics and its Applications, vol. 141, pp. 1–26. Springer.

Garti, N. & Bisperink, C. 1998 Double emulsions: Progress and applications. *Curr. Opin. Colloid Interface Sci.* **3**, 657–667.

Hochmuth, R. M., Tingbeall, H. P., Beaty, B. B., Needham, D. & Transontay, R. 1993 Viscosity of passive human neutrophils undergoing small deformations. *Biophys. J.* **64**, 1596–1601.

Jacqmin, D. 2000 Contact-line dynamics of a diffuse fluid interface. *J. Fluid Mech.* **402**, 57–88.

Johnson, R. E. & Sadhal, S. S. 1985 Fluid mechanics of compound multiphase drops and bubbles. *Annu. Rev. Fluid Mech.* **17**, 289–320.

Kan, H. C., Udaykumar, H. S., Shyy, W. & Tran-Son-Tay, R. 1998 Hydrodynamics of a compound drop with application to leukocyte modeling. *Phys. Fluids* **10**, 760–774.

https://doi.org/10.1017/jfm.2011.235 Published online by Cambridge University Press

Kawano, S., Shirai, A. & Nagasaka, S. 2007 Deformations of thin liquid spherical shells in liquid–liquid–gas systems. *Phys. Fluids* **19**, 012105.

Khatavkar, V. V., Anderson, P. D. & Meijer, H. E. H. 2007 Capillary spreading of a droplet in the partially wetting regime using a diffuse-interface model. *J. Fluid Mech.* **572**, 367–387.

Laugel, C., Rafidison, P., Potard, G., Aguadisch, L. & Baillet, A. 2000 Modulated release of triterpenic compounds from a O/W/O multiple emulsion formulated with dimethicones: infrared spectrophotometric and differential calorimetric approaches. *J. Control. Release* **63**, 7–17.

Mahadevan, L., Adda-Bedia, M. & Pomeau, Y. 2002 Four-phase merging in sessile compound drops. *J. Fluid Mech.* **451**, 411–420.

Muguet, V., Seiller, M., Barratt, G., Ozer, O., Marty, J. P. & Grossiord, J. L. 2001 Formulation of shear rate sensitive multiple emulsions. *J. Control. Release* **70**, 37–49.

Okushima, S., Nisisako, T., Torii, T. & Higuchi, T. 2004 Controlled production of monodisperse double emulsions by two-step droplet breakup in microfluidic devices. *Langmuir* **20**, 9905–9908.

Qian, T. Z., Wang, X. P. & Sheng, P. 2006 A variational approach to moving contact line hydrodynamics. *J. Fluid Mech.* **564**, 333–360.

Ranz, W. E. 1959 Some experiments on the dynamics of liquid films. *J. Appl. Phys.* **30**, 1950–1955.

Rushton, E. & Davies, G. A. 1983 Settling of encapsulated droplets at low Reynolds numbers. *Intl J. Multiphase Flow* **9**, 337–342.

Sadhal, S. S., Ayyaswamy, P. S. & Chung, J. N. 1997 *Transport Phenomena with Drops and Bubbles*. Springer.

Sadhal, S. S. & Oguz, H. N. 1985 Stokes-flow past compound multiphase drops: the case of completely engulfed drops bubbles. *J. Fluid Mech.* **160**, 511–529.

Savva, N. & Bush, J. W. M. 2009 Viscous sheet retraction. *J. Fluid Mech.* **626**, 211–240.

Smith, K. A., Ottino, J. M. & de la Cruz, M. O. 2004 Encapsulated drop breakup in shear flow. *Phys. Rev. Lett.* **93**, 204501.

Stone, H. A. & Leal, L. G. 1990 Breakup of concentric double emulsion droplets in linear flows. *J. Fluid Mech.* **211**, 123–156.

Stroeve, P. & Varanasi, P. P. 1984 An experimental-study on double emulsion drop breakup in uniform shear flow. *J. Colloid Interface Sci.* **99**, 360–373.

Taylor, G. I. 1959 The dynamics of thin sheets of fluid. III. Disintegration of fluid sheets. *Proc. R. Soc. Lond.* A **253**, 313–321.

Utada, A. S., Lorenceau, E., Link, D. R., Kaplan, P. D., Stone, H. A. & Weitz, D. A. 2005 Monodisperse double emulsions generated from a microcapillary device. *Science* **308**, 537–541.

Yap, B. & Kamm, R. D. 2005 Mechanical deformation of neutrophils into narrow channels induces pseudopod projection and changes in biomechanical properties. *J. Appl. Physiol.* **98**, 1930–1939.

Yue, P. T. & Feng, J. J. 2011 Wall energy relaxation in the Cahn–Hilliard model for moving contact lines. *Phys. Fluids* **23**, 012106.

Yue, P. T., Feng, J. J., Liu, C. & Shen, J. 2005 Diffuse-interface simulations of drop coalescence and retraction in viscoelastic fluids. *J. Non-Newtonian Fluid Mech.* **129**, 163–176.

Yue, P. T., Zhou, C. F. & Feng, J. J. 2006*a* A computational study of the coalescence between a drop and an interface in Newtonian and viscoelastic fluids. *Phys. Fluids* **18**, 102102.

Yue, P. T., Zhou, C. F. & Feng, J. J. 2010 Sharp interface limit of the Cahn–Hilliard model for moving contact lines. *J. Fluid Mech.* **645**, 279–294.

Yue, P. T., Zhou, C. F., Feng, J. J., Ollivier-Gooch, C. F. & Hu, H. H. 2006*b* Phase-field simulations of interfacial dynamics in viscoelastic fluids using finite elements with adaptive meshing. *J. Comput. Phys.* **219**, 47–67.

Zhou, C. F., Yue, P. T. & Feng, J. J. 2008 Deformation of a compound drop through a contraction in a pressure-driven pipe flow. *Intl J. Multiphase Flow* **34**, 102–109.

Zhou, C. F., Yue, P. T. & Feng, J. J. 2010 3D phase-field simulations of interfacial dynamics in Newtonian and viscoelastic fluids. *J. Comput. Phys.* **229**, 498–511.

Zosel, A. 1993 Studies of the wetting kinetics of liquid drops on solid surfaces. *Colloid Polym. Sci.* **271**, 680–687.

https://doi.org/10.1017/jfm.2011.235 Published online by Cambridge University Press